Topochemical Reduction of YMnO3 into a Composite Structure

Houria Kabbour, Gilles H. Gauthier, Franck Tessier, Marielle Huvé, Tanguy Pussacq, Pascal Roussel, Michael A. Hayward, Zulma L. Moreno B, Maya Marinova, Marie Colmont, et al.

Topochemical Reduction of $YMnO_3$ into a Composite Structure

Houria Kabbour,[a,*] Gilles Gauthier,[b] Franck Tessier,[c] Marielle Huvé,[a] Tanguy Pussacq,[a] Pascal Roussel,[a] Michael A. Hayward,[d] Zulma L. Moreno B.,[b] Maya Marinova[e], Marie Colmont[a], Silviu Colis,[f] Olivier Mentré [a]

[a] Univ. Lille, CNRS, Centrale Lille, ENSCL, Univ. Artois, UMR 8181 - UCCS - Unité de Catalyse et Chimie du Solide, F-59000 Lille, France

[b] Universidad Industrial de Santander, Grupo INTERFASE, Bucaramanga, Colombia

[c] Institut des Sciences Chimiques de Rennes, Rennes-France

[d] Chemistry Department, University of Oxford-UK

[e] UMET, Université Lille Nord de France, Villeneuve d'Ascq, France

[f] IPCMS, Strasbourg-France

KEYWORDS. Oxides • Topochemistry • Ammonia • Manganese • Composite Structure

ABSTRACT: Topochemical modification methods for solids have shown great potential in generating metastable structures inaccessible trough classical synthetic routes. Here we present the enhanced topotactic reduction of the multiferroic compound $YMnO_3$. At moderate temperature in ammonia flow, the most reduced $YMnO_{3-\delta}$ (δ=0.5) phase could be stabilized. XRD, PND and HREM results show that phase separation occurs into two intimately intergrown layered sublattices with nominal compositions $_\infty[YMn^{2+}O_{2+x}]^{(1-2x)+}$ and $_\infty[YMn^{2+}O_{3-x}]^{(1+2x)-}$ containing versatile Mn^{2+} coordinations. The former sublattice shows original AA stacking between Mn layers while AB stacking in the latter results from oxygen removal from the parent $YMnO_3$ crystal structure.

INTRODUCTION

The controlled modification of inorganic solids in a soft and non-destructive manner constitutes an interesting route to modify their properties, or induce new ones, though subtle structural or compositional adjustments.[1] Recent developments in the manipulation of the anionic array of transition metal oxides, such as topochemical reduction, have allowed the formation of highly unusual structures, in which the redox center combines coordination environments and valence states inaccessible via standard synthesis methods.[2] A striking recent example is $SrFeO_2$, obtained through the reduction of $SrFeO_3$ by metal hydrides, which exhibits infinite layers of square-planar Fe^{2+} [3-4]. A number of other phases containing various transition metals with novel coordination-geometry/oxidation-state combinations have also been reported, such as the $La_{1-x}Ca_xMnO_2$ ($0.6 < x < 1$) series which contain Mn^{1+} [5]; $LaBaCo_2O_{4.25}$ which contains square-planar Co^{1+} [6]; the reduced hexagonal perovskite 4H-$BaMn^{2+}O_{2+x}$ which contains Mn^{2+} centers in a highly unusual array [7] and the square-planar Ni^{1+} containing phase $LaNi^{+}O_2$ [8] On reduction, drastic changes in the physical properties such as the electronic bandgap, magnetic exchange pathways or conductivity are observed.

Studies of the mechanism(s) of reduction of complex oxides are still in their infancy, however initial work investigating the transformation of thin films of the layered brownmillerite $CaFeO_{2.5}$ into $CaFeO_2$ revealed highly anisotropic oxygen diffusion [9] possibly assisted by lattice phonon modes [10]. Evidence and comprehension of such phenomena are important for enhanced oxygen mobility, *e.g.* in the field of catalysis and electrolytes/electrodes for solid oxide fuel cells.

Using these ideas, the hexagonal manganite $YMnO_3$ [11] was recently reduced using CaH_2 at temperatures $225 < T < 350$°C, yielding the partially reduced Mn^{2+}/Mn^{3+} series of phases until $YMnO_{2.80}$. Due to the small size of the rare earth, $YMnO_3$ adopts an acentric hexagonal structure, with respect to the $P6_3cm$ space group [12] rather than the common perovskite form, figure 1a. Its structure consists of sheets of corner-sharing MnO_5 bipyramids (*BPs*) separated by Y^{3+} cations which are arranged in a CdI_2-type sub-lattice. The *BPs* are both cooperatively twisted from the basal *ab*-plane and tilted relative to the *c*-axis to accommodate a mismatch in Mn^{3+}-O and Y^{3+}-O bond lengths. As a result of this distortion, a ferroelectric polarization appears below ~800 K and coexists with antiferromagnetism ($P6'_3$ symmetry [13]) below T_N~ 70 K. The combination of ferroelectricity and (canted) antiferromagnetism means $YMnO_3$ can be described as a type-I magnetoelectric multiferroic, [14] attractive for many applications in magneto-electric and magneto-optical devices. Note that, in the larger family of isostructural hexagonal AMO_3, a deeper structural investigation revealed that the

$YAlO_3$ member, only obtained through the citrate route and often cited as a reference, actually contains carbonate groups [15]. Here, we present the new phase $YMnO_{2.5}$ obtained after maximal topochemical reduction of $YMnO_3$.

EXPERIMENTAL METHODS

Nitrogen and oxygen contents were determined with a Leco TC-600 analyzer using the inert gas fusion method. Nitrogen was detected as N_2 by thermal conductivity and oxygen as CO_2 by infrared detection.

Thermogravimetric analysis (TGA) in air was carried out using a combined TG-DTA 92-1600 SETARAM.

The XRD patterns from fig 1c were obtained on a Bruker AXS D8 Advance X-ray diffractometer (Bragg−Brentano geometry), equipped with a 1D PSD detector (Lynx-Eye), the radiations Cu Kα1,2 were used. The high resolution XRD pattern used for the structure resolution and refinement was collected on a Rigaku Smartlab diffractometer in Bragg-Brentano configuration (equipped with a 9 kW Cu $K_{\alpha 1/\alpha 2}$ rotating anode).

Transmission electron Microscopy (TEM) experiments were carried out on a FEI Technai G220.

Powder neutron diffraction (PND) data were collected on the 3T2 diffractometer, λ=1.22 Å (Laboratoire Leon brillouin, Saclay, france)

SHG (Second Harmonic Generation) measurements were carried out using a laser scan microscope LSM 710 NLO Zeiss (Iena, Germany). The beam was generated by a laser CHAMELEON femtosecond Titanium-Sapphire (Coherent, Santa Clara, USA) regulated at 900nm.

RESULTS AND DISCUSSION

The reduction of the precursor $YMnO_3$ was achieved at 600°C under NH_3 gas flow for 8 hours, in a treatment more commonly used to form oxy-nitrides, e.g. $LaTaON_2$ from $LaTaO_4$ [16]. The basic action of ammonia is based on its decomposition at high temperature (>500°C) into active nitrogen species and molecular hydrogen: $NH_3 \rightarrow \frac{1}{2}N_2 + \frac{3}{2}H_2$. While hydrogen reacts with the oxygen atoms of the solid, the nitrogen may be incorporated in the resulting oxygen vacancies [17]. In our conditions however, NH_3 acts as a powerful and soft reducing agent leading to the removal of 1/6th of the initial oxygen content, not achieved by other routes. Furthermore, in contrast to the hydride topotactic reduction route which produces solid by-products such as CaO or NaOH [4, 18] requiring a further separation procedure, the use of NH_3 is clean and straightforward.

X-ray powder diffraction (XRD) pattern (Figure 1) of $YMnO_3$ heated at 600 °C under flowing ammonia is reminiscent of the unreduced phase, but with significant changes of the relative intensities and vanishing of several reflections, consistent with the occurrence of a topochemical modification. Close inspection of the XRD data revealed the presence of minor traces of Y_2O_3 and MnO, indicative of a small amount of sample decomposition, clue that 600 °C is the temperature limit for topochemical reduction. At 800°C, the ammonolysis treatment leads to a full decomposition of the sample into Y_2O_3 and MnO. The lack of nitrogen in samples was confirmed by combustion analysis. First, it is important to mention that no evidence of OH^- is detected by IR measurements (see Fig. 1c) and that nitrogen is excluded by combustion analysis. Their absence is also confirmed by powder neutron diffraction (PND) as will be discussed later.

Thermogravimetric re-oxidation plot upon heating of the reduced sample at 5 K/min in air (Figure 1b) shows a mass uptake of ~5.6% between 200 and 400°C together with a sharp DTA peak, in good agreement with the $YMnO_{2.5}$ formula, when the over stoichiometry of oxidized $YMnO_{3+\delta}$ (i.e. δ = 0.11) is taken into account, see also S1. Details on the location of the oxygen over-stoichiometry in $YMnO_{3+\delta}$ are discussed in reference [19]. Further heating of the sample in air leads to a mass loss at 700°C (1.5%), typical of the manganese self-reduction at high temperature back to stoichiometric $YMnO_3$. In combination these observations validate a final oxidation state of Mn^{2+} for the reduced phase with reversible oxygen reincorporation, as shown from the XRD of the $YMnO_{2.5}$ air-TGA residue (Figure 1b).

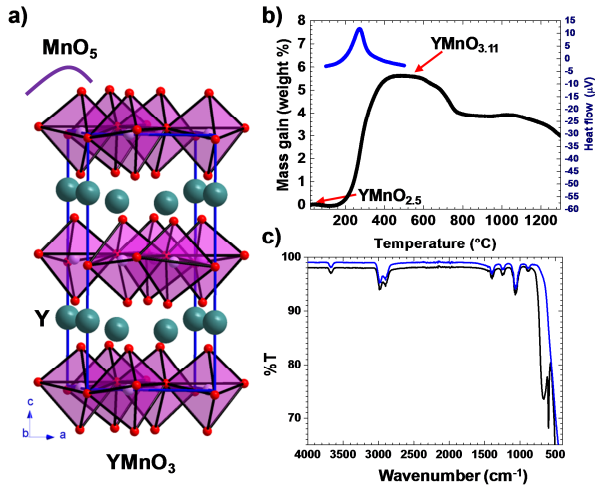

FIGURE 1. (a) Crystal structure of the precursor $YMnO_3$. (b) TGA in air (black) and DTA (blue) of $YMnO_{2.5}$. (c) IR spectra for the reduced $YMnO_{2.5}$ (blue) and for the precursor $YMnO_3$ (black)

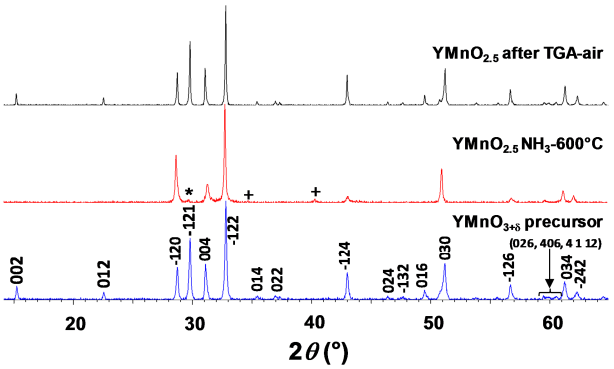

FIGURE 2. The XRD patterns of the precursor, the reduced phase $YMnO_{2.5}$ and after its TGA-air. "*" points the unique minor peak which would involve the c-doubling, also falling at the (-121) $YMnO_3$ 2θ angle. "+" point MnO impurity.

The powder XRD pattern of $YMnO_{2.5}$ can be fully indexed in a simple hexagonal unit cell with a = 3.5671(1) Å and c =

5.6728(1) Å. This corresponds to the relationship a' = a/√3, c' = c/2 relationship with the unit cell of $YMnO_3$, with a V/6 volume reduction. However, at this stage an extra minor peak at d= 2.97 Å, could either be assigned to the (-121) reflection of residual unreacted $YMnO_3$, either involve a doubling of c' (011) for c'=c_{YMnO3}). This tiny ambiguity dealing with XRD data will turn into crucial after consideration of powder neutron diffraction (PND) data.

The average structure of the reduced phase$YMnO_{2.5}$ was solved using the charge flipping procedure as implemented in the Jana2006 suite [20] and using a high resolution XRD pattern (see Methods). Rietveld refinements and Fourier differences maps were combined to achieve a mean structural model in various trigonal or hexagonal symmetries. Finally, the centric *P*6/*mmm* space group (Table 1 and S3) gives best reliability factors (R_{Bragg}=0.0719, goodness of fit= 3.16) together with the best picture of the average model over a strongly disordered crystal structure. The observed, calculated and difference patterns are plotted in S2.

Table 1. Atomic positions of $YMnO_{2.5}$ and isotropic displacement parameters (Å²) in *P*6/*mmm*, a= 3.5671(1) Å and c = 5.6728(1) Å. Y1 is half occupied while the rest is scaled respectively.

Atom	Wyck.	x	y	z	Occupancy	U_{iso} (Å²)
Y1	1b	0	0	1/2	0.5	0.0080(8)
Y2	2e	0	0	0.6116(10)	0.25	0.053(2)
O1	2e	0	0	0.0946(18)	0.5	0.005(3)
O2a	4h	1/3	2/3	0.345(4)	0.2812	0.105(6)
O2b	4h	1/3	2/3	0.766(15)	0.0938	0.105(6)
Mn1	2d	2/3	1/3	0	0.5	Aniso.[a]

[a] See S4

The XRD-refined structure of $YMnO_{2.5}$, shown in Figure 3, exhibits a very large amount of disorder, with all atomic positions having partial occupancy (Table S4a). One can deconvolute the refined disordered model into an intergrowth of ordered layers, by observing that the two manganese positions (1/3, 2/3, 0) and (2/3, 1/3, 0) with d(Mn-Mn) =2.06 Å form two imbricated lattices, which cannot be simultaneously occupied – a feature which is also true for the Y1 and Y2 positions. Note that our tests in less symmetric space groups (P3 for instance) systematically showed the co-existence of these two sub-arrays in inequivalent positions. Furthermore the refined oxygen positions O1 and O2a/O2b correspond approximately to the 'equatorial' and 'axial' anion sites of the MnO_5 bipyramids of the $YMnO_3$ parent phase (see S6 for further description).

Using this idea, two ordered sub-lattices can be constructed as shown in Figure 3. The first one roughly corresponds to the $YMnO_3$ crystal structure formed of $_\infty[Y1Mn^{2+}O_{3-x}]^{(1+2x)-}$ deficient layers. It leads to coordination 5-*n* (*BP*$_{-n}$) for Mn. Manganese centers are surrounded by three (maximum) O1 'equatorial' anions and two O2a 'axial' anions (Figure 2c). The hexagonal sheets of bipyramids should stack in an ABAB manner along the c-axis, with Y^{3+} cations occupying the octahedral (CdI_2 type) coordination sites made by the O2a anions, between the Mn-O sheets. The ideal ABAB stacking sequence leads to the alternation between the (1/3, 2/3, 0) and (2/3, 1/3, 0) Mn sites in juxtaposed layers. However, this simple "*$YMnO_{3-x}$ like vision*" does not picture the experimental observation of imbricated sub-lattices in a single cell along c.

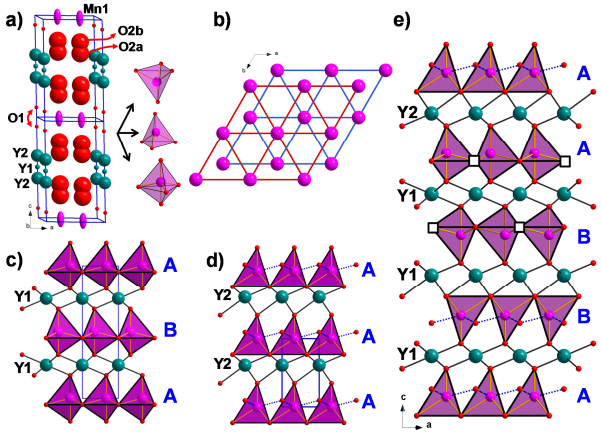

FIGURE 3. a) XRD Refined $YMnO_{2.5}$ model with labels. Built *BP* and *Td* have realistic Mn-O distances as described in the supporting information. b) View of the two imbricated Mn sublattices shown by blue and red Mn-Mn bonds. c) $_\infty[YMn^{2+}O_{3-x}]^{(1+2x)-}$ (ABAB stacking) and d) $_\infty[YMn^{2+}O_{2+x}]^{(1-2x)+}$ (AAA stacking) ordered sublattices built from atomic positions of a). e) Different combinations based on the two sublattices. The white filled squares represent possible vacancies.

To solve the problem, a second sub-lattice with the $_\infty[Y2Mn^{2+}O_{2+x}]^{(1-2x)+}$ composition has to be imagined, conserving the inalterable CdI_2 layers around Y2. Each manganese center form tetrahedral (*Td*) with three basal O2b anions, one apical O2a anion. This coordination can be completed by O1 anions that allow the coordination around Mn to vary as Td_{+n}, to form variable order polyhedra (Figure 2d). These sheets ideally stack in a primitive AA manner in a single cell (c/2). Y^{3+} (Y2) occupy octahedral coordination sites formed by O2a and O2b. This sublattice corresponds to an artificially built novel $YMnO_{2+x}$ hexagonal polytype in *P*3*m*1 space group with original AA stacking sequence between the Mn layers, see details in S4. Finally, in the bulk $YMnO_{2.5}$, the observed stoichiometry of $YMnO_{2.5}$ results from the disordered stacking of $_\infty[YMn^{2+}O_{2+x}]^{(1-2x)+}$ and $_\infty[YMn^{2+}O_{3-x}]^{(1+2x)-}$ sub-lattices. Of course in the compound, all Y^{3+} ions occupy CdI_2 triangular layers, leading to the modular slicing into $[YO_2]^-[MnO_{1-x}]^{(-2x)-}[YO_2]^-$ $[MnO_x]^{(2-2x)+}$ sub-units, with disordered Mn-based layers.

In order to verify the reality of our novel sublattice within a disordered composite model, electron diffraction (ED) data and high resolution transmission electron microscope (HRTEM) images were collected. Figure 4a shows the [001] zone axis pattern of $YMnO_{2.5}$, which can be readily indexed in the unit cell given by powder XRD (a'= $a_{YMnO3}/\sqrt{3}$). In contrast the [010] zone axis pattern contains diffuse streaks containing weak *h*0*l* (*l*=*n*/2) supercell spots, not observed in the XRD data, fig. 4b. Their presence is consistent with the local doubling of the c-axis required for ABAB stacking.

HREM images of the [010] zone further confirm this picture. Figure 4c shows a simulated image of ABAB stacking between *BP* layers, corresponding to the $_\infty[YMn^{2+}O_{3-x}]^{(1+2x)-}$-type sub-structure for a defocus of 0 Å and a thickness of 21.4 Å. Figure 4d shows the corresponding simulation for the AAA stacking block with the $_\infty[YMn^{2+}O_{2+x}]^{(1-2x)+}$-type sub-structure in same conditions. Bright spots correspond to the cation positions, which are highlighted in green (Y) and purple (Mn) on the image. Using these simulated images as a guide, the inter-

pretation of the HREM [010] zone axis images is unambiguous, see Figure 4e. It corresponds to an irregular sequence between AA (or BB) and AB stacking modes. By examining various stack possibilities between [$YMnO_{3-x}$]-type BP_{+n} layers and [$YMnO_{2+x}$]-type Td_{-n} layers, see Figure 2e, we found that AA (or BB) stacking can be formed at the Td_{+n}/Td_{+n} and Td_{+n}/BP_{-n} interfaces while AB stacking can be formed at the BP_{-n}/BP_{-n} , Td_{+n}/BP_{-n} and even at the Td_{+n}/Td_{+n} at both sides of an antiphase boundary. Therefore, it is not possible to assign the specific identity of any Mn-O sheet in the experimental HREM image. At least, the evidence of a majority of AA stacking involve greater concentration of $_{\infty}[YMn^{2+}O_{2+x}]^{(1-2x)+}$ fragments, i.e. with Td_{+n} coordination while $_{\infty}[YMn^{2+}O_{3-x}]^{(1+2x)-}$ with BP_{-n} is less represented. It sounds that the versatile arrangements between these two types of deficient layers, and the plausible distribution of oxygen stoichiometry in each individual ones would be the driving force for the disordered composite features of $YMnO_{2.5}$.

The main features from our XRD study are consistent with the subsequent Rietveld refinement using powder neutron diffraction (PND). Here one must mention the real difficulty to reach a plausible and converging model within acceptable agreement factors, due to the oxygen disorder. It probably contributes to the high measured background together with the small amount of collected compound (*ca.*1g). However, the background is also characterized by more or less intense broad bumps that generally indicate static interatomic correlations due to diffuse elastic scattering. The Debye function Q =(2π x 1.23)d is used and gives typical interatomic distances at their origin, as commonly used to deduce O-O pair distance along diffusion in oxygen conductors [21]. The first bump centered at Q_{max} = 4π sinθ/λ = 2.57 $Å^{-1}$ gives d=3.0Å which is a typical O-O distance inside Td_{+1} or Bp_{-1} polyhedrons and comfort short range correlations. Tables with atomic positions and thermal parameters are given in S7. The experimental pattern is given figure 5a. Its main particularity consists in the appearing of diffraction peaks which imply the conservation of the original c-axis, contrarily to what is observed from XRD, but consistently with weak ED satellites (see fig. 4a). The inset of the figure 4a highlights the weak (101) and intense (103) reflections, after refinement of the lattice parameters a= 3.5666(3) Å and c=11.3493(5) Å. Despite the presence of two individual blocks in the c-doubled unit cell, in any tested groups, the imbrication of the two Mn sublattices (see fig.3b) on each layer was confirmed together with the disorder on yttrium positions, similarly to our XRD observations. The Yttrium was finally modelled using a central position with exaggerated anisotropic thermal parameter elongated along c.

Keeping these features in mind, the (PND) c-doubling involve that two next [MnO_x] layers are distinct and correlated in space, but with sufficiently imperfect ordering to be imperceptible by XRD.

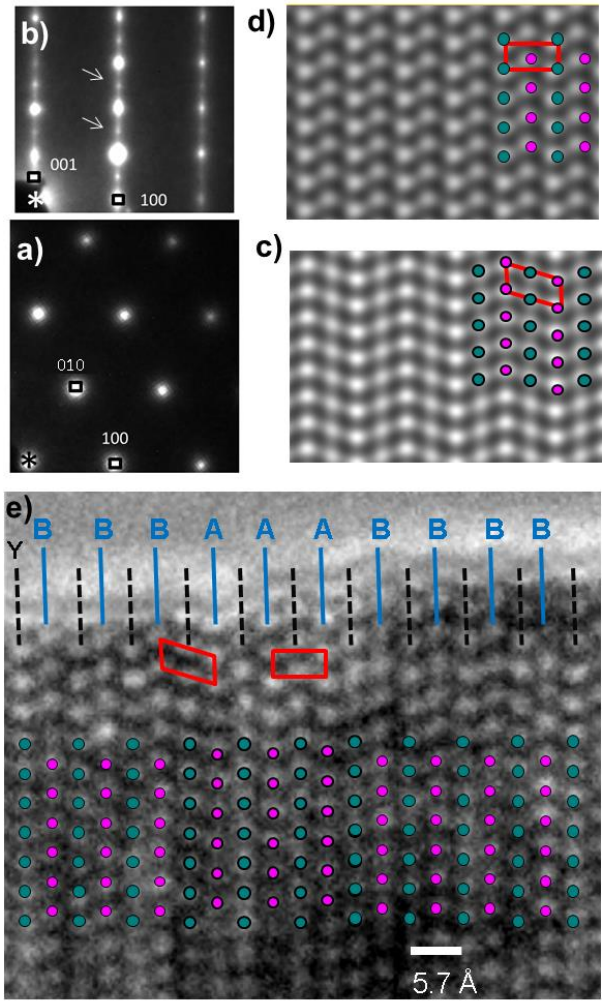

FIGURE 4. a) and b) TEM images obtained for the reduced phase $YMnO_{2.5}$. c) and d) Simulated high resolution TEM images for $YMnO_3$ and $YMnO_2$ models respectively. e) Experimental HRTEM image with the stacking type superimposed. Models in fig. 2c-d were used for the HREM simulations. Figure e) is also presented in S6 without annotations for clarity.

Such features refute the accurate localization of the full anionic sublattices, but a plausible model was refined in the *P*-31*m* space group after a large number of trials (by varying the symmetry, considering or not disordered fragments in the structure, treatment of multiphased or single phased $YMnO_{3-\delta}$ components *etc*…) leading to R_{Bragg}= 7.35 % for $YMnO_{2.5}$ main phase(89 wt.%), R_{Bragg}= 5.14 % for MnO impurity (3.4 wt.%) and R_{Bragg}= 20.6 % for Y_2O_3 impurity (7.6 wt.%). We find one independent yttrium (at z= 0.21 and 0.79) and two independent Mn (Mn1 at z= 0 and Mn2 at z= 0.5). Once again, it confirms the XRD vision, i.e. a regular Mn sub-array defining the unit cell, in which Y^{3+} is locally off centered. The refined cation surrounding is complex and differs between two subsequent layers, in average, see figure 5 with details and the oxygen refined occupancies. Here oxygen were labelled as O1a,b,c and O2a,b,c,d as satellites of the O1 and O2a,b positions from our XRD refinement. *In fine*, when summing the oxygen contribution, two distinct layers are stacked along the c-axis, [$MnO_{2.06}$] and [$MnO_{2.95}$], which pictures a pseudo or-

dering between oxygen poor (BP_{-1}, Td, Td_{+1}) and oxygen rich (BP, Td_{+1}, Td_{+2}) layers along c. In this composite phase, even after reliable PND refinement the identification of clear MnO_x polyhedra was not possible. At least, the distinction of a variety of coordination which involves all the located oxygen positions is proposed figure 5c and d. In reality, a higher disorder is of course expected between AA and AB types with various geometries of the MnO_x polyhedra. Dealing with symmetries, it is clear that nor P6/mmm (simple cell, XRD), neither *P*-31*m* (double cell, PND) reflect the true structure, but only allow refining the main composite structure. At best can we say that it is formed from the intergrowth between two end-members with symmetries $P6_3cm$ ($YMnO_{3-x}$, double cell) and *P*3m1 ($YMnO_{2+x}$, simple cell), see also S4 for the later.

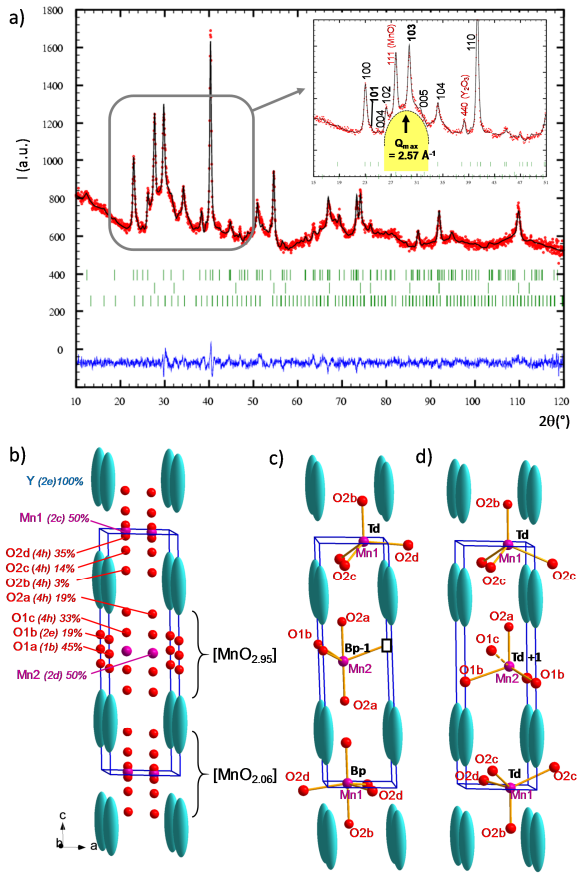

FIGURE 5. a) Results of the PND Rietveld refinement (R_{Bragg} $YMnO_{2.5}$ = 7.35 %). b) Refined model with distinct MnO_x layers. c) and d) Possible Mn coordination (arranged in layers built from b).

The refined structure of $YMnO_{2.5}$ presented here differs significantly from that of $YMnO_{2.80}$ [11] prepared by reduction with CaH_2. $YMnO_{2.80}$ is strongly related to stoichiometric $YMnO_3$ crystal structure (AB stacking) in which the BP_{-1} anion vacancies are located in 'equatorial' anion sites. In contrast the structure of $YMnO_{2.5}$ incorporates a predominant amount of AA stacking, each involving at least one pseudo-tetrahedral Td_{+n} layers, see figure 3e. It suggests that the segregation of tetrahedra into layers occur for exaggerated oxygen sub-stoichiometry, leading to brutal stacking changes, *i.e.* strong reorganization/shift between the Mn layers. The smooth conversion of $YMnO_3$ into $YMnO_{2.80}$ by simple anion removal is not possible anymore on further reduction until $YMnO_{2.5}$. Two distinct reduction regimes occur with conservation or not of the original AB stacking, and imply a high and scalable degree of anion mobility for all the anion sites in the system. Indeed, $YMnO_{2.5}$ is logically disordered, sitting at the extreme reduction side of $YMnO_3$ with participation of novel sub-units, while an increasing disorder is reported along the non-stoichiometric $YMnO_{3-\delta}$ series with δ= 0, 0.05, 0.15, and 0.20. [11]

This result is highlighted by the SHG signal measured on reduced $YMnO_{3-\delta}$ on increasing δ. Results are shown on the figure 6a-c using in reflection mode femtosecond excitations at 900 nm (titanium-sapphire laser). Samples have been sealed under argon in Pyrex capillaries to avoid re-oxidation. The colored surface reveals the SHG emitting surface (micrometric resolution). As expected, $YMnO_3$ is SHG emitter while $YMnO_{2.8}$ (re-prepared in the conditions of reference [11]) shows a more dilute distribution of emitting domains although the average structure was refined in the $P6_3/mmc$ centrosymmetric space group. It shows locally domains that preserve the initial polar oxygen arrangement. For $YMnO_{2.5}$ the SHG signal is absent which proves the vanishing of the dipolar momentum at the nanometric scale by intimate disorder between layers.

The $YMnO_{2.5}$ formula and Mn^{2+} oxidation state are further supported by spectroscopic studies as shown in figure 6d with EELS spectra at O-*K* and Mn-$L_{2,3}$ edges for $YMnO_3$ and reduced $YMnO_{2.5}$. The observed shift of the L_3 peak position toward lower energies for the reduced phase is consistent with a reduction of the Mn oxidation state as already discussed in the literature [22]. Moreover, our shift value of 2.1 eV from Mn^{3+} to Mn^{2+} is consistent with similar reported shifts for $Mn^{3+}\rightarrow Mn^{2+}$. [22a] The significant changes of the O-*K* edges are also consistent with the structural variation around O atoms after reduction.

Around 10-15 K, the magnetic susceptibility of $YMnO_{2.5}$ seems to exhibit a local maximum (fig. 6e) together with a ZFC/FC divergence which could sign canted or uncompensated magnetic moments over antiferromagnetic (AFM) interactions. The magnetization measured at 2K (inset fig.4b) shows a weak remanent moment of ~5.10^{-3} μ_B/FU. $YMnO_{2.80}$ [11], exhibit similarly a local maximum in the zero field cooled data at slightly higher temperature ~20 K. Our phase may behave like $YMnO_{2.85}$ and $YMnO_{2.80}$ in which the magnetic ordering vanishes for a spin-glass state due to the high structural and valence disorder. However the conservation of ordered in-plane Mn^{2+} lattices could be responsible for 2D magnetic correlations evidenced below 15K. The weak anomaly around 70 K is assigned to the AFM ordering of the unreacted amount of precursor (T_N~ 70K) identified from XRD.

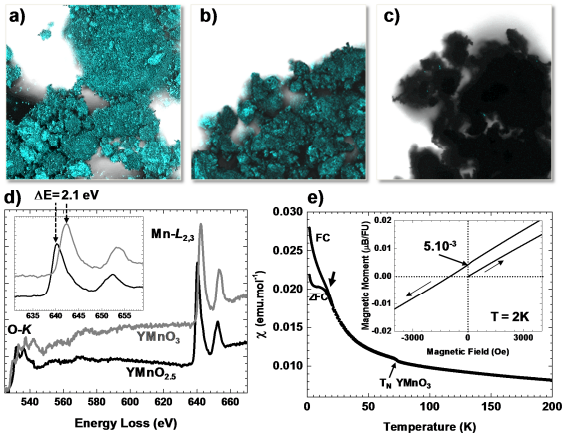

FIGURE 6. a) SHG measurements for the precursor $YMnO_3$, b) for the intermediate reduced phase $YMnO_{2.8}$ and c) for our reduced phase $YMnO_{2.5}$. All blue pixels correspond to surficial area emitting the doubling frequency. d) O-*K* and Mn-$L_{2,3}$ edge spectra from $YMnO_3$ and reduced $YMnO_{2.5}$ after background subtraction with an inset showing a zoom highlighting the energy shift. e) Magnetic susceptibility with temperature and magnetization (inset).

An effective moment of ~6.7 μB was found from the Curie-weiss fit in good agreement with a spin-only contribution of Mn^{2+}. In addition, a redox titration protocol consisting in a retro-titration of Mn^{3+} ions showed the absence of Mn^{3+} ions which comfort the reduction down to Mn^{2+} (see S8).

CONCLUSION

In summary, we have achieved the extreme reduction of the well-known multiferroic material $YMnO_3$. Using ammonia at moderate temperature, the green-colored phase $YMnO_{2.5}$, exhibiting only Mn^{2+}, as supported by several techniques (TGA, EELS, magnetism and redox titration), could be stabilized. The highly disordered structure consisting of an intergrowth of two different layer types can be seen as an extreme structural adaptation to satisfy all the coordination 'requirements' of all the atoms in the system upon massive oxygen removal. HREM show regions with AA and AB stacking of the Mn layers while Y layers show only AA stacking. In addition, the highly anion-deficient and disordered $YMnO_{2.5}$ phase should be quite reactive toward other anions filling, e.g. fluorine, using adapted topochemical reactions. It should greatly impact the structure and the properties (nature and strength of magnetic interactions *etc*…). The phase $YMnO_{2.5}$ is certainly a fascinating compound appealing for deeper comprehension.

ASSOCIATED CONTENT

Supporting Information. TGA-H_2 (S1), refinement (S2), anisotropic thermal parameters and ordered model (S3), atomic positions of sub-lattice $YMnO_{2+x}$, (simple cell) (S4), HREM without annotations (S5), further structure description (S6). In (S7) are the details of the PND refinement and structural parameters, in (S8) the redox titration. "This material is available free of charge via the Internet at http://pubs.acs.org."

AUTHOR INFORMATION

Corresponding Author

* houria.kabbour@univ-lille1.fr

Funding Sources

Agence Nationale de la Recherche with ANR project ANION-CO (12-JS08-0012)

ACKNOWLEDGMENT

This work was carried out under the framework of the ANR project ANION-CO (12-JS08-0012). X-Rays Diffractometers are funded by Région NPDC, FEDER, CNRS and MESR. TEM facility is supported by Région NPDC, ERDF and INSU-CNRS. Christine Terryn is thanked for SHG measurements. Florence Porcher is thanked for Neutron Diffraction Data Collection.

REFERENCES

[1] Hayward, M. A. Soft Chemistry Synthesis of Oxides in *Comprehensive Inorganic Chemistry II*, Vol. 2 (Eds. J.Reedijk and K.R. Poeppelmeier) Elsevier, Oxford, **2013**, 417.

[2] Hayward, M. A.; Rosseinsky, M. J. Anion Vacancy Distribution and Magnetism in the New Reduced Layered Co(II)/Co(I) Phase $LaSrCoO_{3.5-x}$. *Chem. Mater*. **2000**, *12*, 2182–2195. Hayward, M. A.; Cussen, E. J.; Claridge, J. B.; Bieringer, M.; Rosseinsky, M. J.; Kiely, C. J.; Blundell, S. J.; Marshall, I. M.; Pratt, F. L. The Hydride Anion in an Extended Transition Metal Oxide Array: $LaSrCoO_3H_{0.7}$. *Science* **2002**, *295*, 1882.

[3] Tsujimoto, Y.; Tassel, C.; Hayashi, N.; Watanabe, T.; Kageyama, H. ; Yoshimura, K.; Takano, M.; Ceretti, M.; Ritter, C.; Paulus, W. Infinite-layer Iron Oxide with a Square-planar Coordination. *Nature* **2007**, *450*, 1062-1065.

[4] Tassel, C. ; Watanabe, T. ; Tsujimoto, Y.; Hayashi, N.; Kitada, A.; Sumida, Y.; Yamamoto, T.; Kageyama, H.; Takano, M.; Yoshimura, K. Stability of the Infinite Layer Structure with Iron Square Planar Coordination. *J. Am. Chem. Soc*. **2008**, *130*, 3764-3765.

[5] Dixon, E.; Hadermann, J. ; Ramos, S. ; Goodwin, A. L.; Hayward, M. A. Mn(I) in an Extended Oxide: The Synthesis and Characterization of $La_{1-x}Ca_xMnO_{2+\delta}$ ($0.6 \leq x \leq 1$). *J. Am. Chem. Soc*. **2011**, *133*, 18397–18405.

[6] Seddon, J.; Suard, E.; Hayward, M. A. Topotactic Reduction of $YBaCo_2O_5$ and $LaBaCo_2O_5$: Square-Planar Co(I) in an Extended Oxide. *J. Am. Chem. Soc*. **2010**, *132*, 2802–2810.

[7] Hadermann, J.; Abakumov, A. M.; Adkin, J. J.; Hayward, M. A. Topotactic Reduction as a Route to New Close-Packed Anion Deficient Perovskites: Structure and Magnetism of 4H-$BaMnO_{2+x}$. *J. Am. Chem. Soc*. **2009**, *131*, 10598-10604.

[8] Hayward, M. A.; Green, M. A; Rosseinsky, M. J.; Sloan, J. Sodium Hydride as a Powerful Reducing Agent for Topotactic Oxide Deintercalation: Synthesis and Characterization of the Nickel(I) Oxide $LaNiO_2$. *J. Am. Chem. Soc*. **1999**, *121*, 8843-8854

[9] Inoue, S.; Kawai, M.; Ichikawa, N.; Kageyama, H.; Paulus, W.; Shimakawa, Y. Anisotropic Oxygen Diffusion at Low Temperature in Perovskite-Structure Iron Oxides. *Nature Chem.* **2010**, *2*, 213-217

[10] Paulus, W.; Schober, H.; Eibl, S.; Johnson, M.; Berthier, T.; Hernandez, O.; Ceretti, M.; Plazanet, M.; Conder, K.; Lamberti, C. Lattice Dynamics To Trigger Low Temperature Oxygen Mobility in Solid Oxide Ion Conductors. *J. Am. Chem. Soc.* **2008**, *130*, 16080-16085

[11] Overton, A. J.; Best, J. L.; Saratovsky, I.; Hayward, M. A. Influence of Topotactic Reduction on the Structure and Magnetism of the Multiferroic $YMnO_3$. *Chem. Mater*. **2009**, *21*, 4940–4948.

[12] Jeong, I.-K.; Hur, N.; Proffen, Th. High-temperature structural evolution of hexagonal multiferroic $YMnO_3$ and $YbMnO_3$. *Journal of Applied Crystallography* **2007**, *40*, 730-734.

[13] Varignon, J.; Petit, S.; Gelle, A. ; Lepetit, M. B. An *Ab initio* Study of Magneto-Electric Coupling of $YMnO_3$. *J. Phys. Condens. Matter*. **2013**, *25*, 496004

[14] Eerenstein, W.; Mathur, N. D.; Scott, J. F. Multiferroic and Magnetoelectric Materials. *Nature* **2006**, *442*, 759.

[15] Li, J.; Smith, A. E.; Jiang, P. ; Stalick, J. K.; Sleight, A. W.; Subramanian, M. A.. True Composition and Structure of Hexagonal "$YAlO_3$", Actually $Y_3Al_3O_8CO_3$. *Inorganic Chemistry* **2015**, *54*, 837-844

[16] Clark, L.; Oro-Sole, J.; Knight, K.S.; Fuertes, A.; Attfield, J. P. Thermally Robust Anion-Chain Order in Oxynitride Perovskites. *Chem. Mater*. **2013**, *25*, 5004−5011

[17] Tessier, F.; Marchand, R. Ternary and Higher Order Rare-Earth Nitride Materials: Synthesis and Characterization of Ionic-Covalent Oxynitride Powders. *J. Solid State Chem.* **2003**, *171*, 143-151.

[18] Hyett, G.; Barrier, N.; Clarke, S. J.; Hadermann, J. Topotactic Oxidative and Reductive Control of the Structures and Properties of Layered Manganese Oxychalcogenides. *J. Am. Chem. Soc.* **2007**, *129*, 11192-11201.

[19] Abughayada, C.; Dabrowski, B.; Avdeev, M.; Kolesnik, S.; Remsen, S.; Chmaissem, O. Structural, magnetic, and oxygen storage

properties of hexagonal $Dy_{1-x}Y_xMnO_{3+\delta}$. *J. Solid State Chem.* **2014**, *217*, 127-135

[20] Petricek, V.; Dusek, M. ; Palatinus, L. *JANA2006*, Institute of Physics, Academy of Sciences, Praha, Czech Republic, **2006**.

[21] Vannier, R.N.; Abraham, F.; Nowogrocki, G.; Mairesse, G. *J. Solid State Chem.* **1999,** *142*, 294-304

[22] a) Kurata, H.; Colliex, C. Electron-Energy-Loss Core-Edge Structures in Manganese Oxides. *PRB* **1993**, *48*, 2102-2109. b) Laffont, L.; Gibot, P. High Resolution Electron Energy Loss Spectroscopy of Manganese Oxides: Application to Mn_3O_4 Nanoparticles. *Materials characterization* **2010**, *61*, 1268-1273

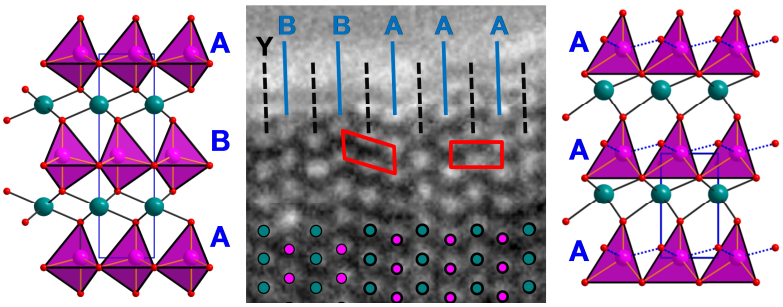

Topochemical reduction of $YMnO_3$ generates the highly oxygen deficient $YMnO_{3-\delta}$ (δ=0.5) compound exibiting microscopic phase separation into two intergrown layered sublattices with nominal compositions of $_{\infty}[YMn^{2+}O_{2+x}]^{(1-2x)+}$ and $_{\infty}[YMn^{2+}O_{3-x}]^{(1+2x)-}$.